

## Article

# Electrospun Fibrous Nanocomposite Sensing Materials for Monitoring Biomarkers in Exhaled Breath

Yin-Hsuan Chang <sup>1</sup>, Ting-Hung Hsieh <sup>1</sup>, Kai-Chi Hsiao <sup>1</sup>, Ting-Han Lin <sup>1</sup>, Kai-Hsiang Hsu <sup>2,\*</sup>   
and Ming-Chung Wu <sup>1,2,3,\*</sup> 

<sup>1</sup> Department of Chemical and Materials Engineering, Chang Gung University, Taoyuan 33302, Taiwan

<sup>2</sup> Division of Pediatric Neonatology, Department of Pediatrics, Chang Gung Memorial Hospital, Linkou, Taoyuan 33305, Taiwan

<sup>3</sup> Green Technology Research Center, Chang Gung University, Taoyuan 33302, Taiwan

\* Correspondence: khsu@cgmh.org.tw (K.-H.H.); mingchungwu@cgu.edu.tw (M.-C.W.)

**Abstract:** Human-exhaled breath mainly contains water, oxygen, carbon dioxide, and endogenous gases closely related to human metabolism. The linear relationship between breath acetone and blood glucose concentration has been revealed when monitoring diabetes patients. Considerable attention has been directed toward developing a highly sensitive volatile organic compounds (VOCs) sensing material that can detect breath acetone. In this study, we propose a tungsten oxide/tin oxide/silver/poly (methyl methacrylate) (WO<sub>3</sub>/SnO<sub>2</sub>/Ag/PMMA) sensing material fabricated using the electrospinning technique. By monitoring the evolution of sensing materials' extinction spectra, low concentrations of acetone vapor can be detected. Moreover, the interfaces between SnO<sub>2</sub> and WO<sub>3</sub> nanocrystals construct n–n junctions, which generate more electron–hole pairs than those without such structure when the light strikes. This helps to improve the sensitivity of sensing materials when they are subjected to acetone surroundings. The established sensing materials (WO<sub>3</sub>/SnO<sub>2</sub>/Ag/PMMA) exhibit a sensing limit of 20 ppm for acetone vapor and show specificity for acetone even in ambient humidity.

**Keywords:** electrospinning; exhaled breath sensors; diabetes; acetone sensor



**Citation:** Chang, Y.-H.; Hsieh, T.-H.; Hsiao, K.-C.; Lin, T.-H.; Hsu, K.-H.; Wu, M.-C. Electrospun Fibrous Nanocomposite Sensing Materials for Monitoring Biomarkers in Exhaled Breath. *Polymers* **2023**, *15*, 1833. <https://doi.org/10.3390/polym15081833>

Academic Editor: Andrea Pucci

Received: 12 February 2023

Revised: 2 April 2023

Accepted: 6 April 2023

Published: 10 April 2023



**Copyright:** © 2023 by the authors. Licensee MDPI, Basel, Switzerland. This article is an open access article distributed under the terms and conditions of the Creative Commons Attribution (CC BY) license (<https://creativecommons.org/licenses/by/4.0/>).

## 1. Introduction

Diabetes is recognized as one of the fastest-growing diseases and is one of the top ten causes of death globally in the 21st century. Predictions suggest the number of diabetes patients worldwide will increase to 643 million by 2030 and 783 million by 2045 [1]. Diabetic ketoacidosis (DKA) is an acute metabolic complication in type 1 diabetes mellitus, which is due to the deficiency of insulin. Blood glucose level is an important clinical diagnosis for diabetes, which requires routine blood glucose monitoring to inform recommendations for adjustments related to diet, medication, and exercise regimens [2–4]. Besides, inadequate insulin results in the decomposition and oxidation of free fatty acids, leading to increased ketone in the blood [5,6]. Therefore, acetone in the breath can be seen as a significant biomarker for diabetes as an alternative to traditional finger-pricking to monitor blood glucose [7–9].

Human-exhaled breath mainly contains 78% nitrogen, 16% oxygen, 4% carbon dioxide, 0.09% argon and over 3500 volatile organic compounds (VOCs) [10–12]. After the inhaled air goes into the alveoli in the lungs, molecules pass the blood–air barrier, allowing the excretable metabolic products to be excreted in the exhaled breath. Therefore, the exhaled breath can represent the endogenous metabolic fingerprint [13,14]. For healthy people, breath acetone concentrations range from 0.3 ppm to 0.9 ppm. Diabetes can be identified once the breath acetone concentration exceeds 1.8 ppm. Owing to this relationship, developing a cost-effective and reliable exhaled breath sensing device is urgent. Currently, a variety of acetone detection methods have been reported, including colorimetric sensors [15,16], optical sensors [17,18], metal oxide sensors [8,19], monolayer-coated metal

nanoparticle sensors [20], etc. Liao et al. demonstrated the detection of acetone using a luminescent chemosensor. When europium (Eu)–containing covalent organic framework (DhaTab–COF–EuIL) was exposed to acetone, it revealed significant luminescence quenching toward acetone caused by competitive absorption of the light source’s energy and led to the transfer of photoinduced energy [21]. In 2021, Wang et al. updated the possibility of using colorimetric sensors to track breath acetone accurately. The protons produced by the reaction between acetone and hydroxylamine sulfate induced the pH change and visualized the existence of acetone through color changes [22].

A wide variety of sensing materials, including conjugating polymers [23,24], metal–organic frameworks [25,26], and semiconductor materials [27,28] have been utilized for sensing volatile organic compounds (VOCs). Tungsten trioxide ( $\text{WO}_3$ ) has attracted considerable attention as a gas–sensing material due to its gasochromic properties, high stability, and high sensitivity. Likewise, tin oxide ( $\text{SnO}_2$ ), an n–type semiconducting metal oxide, has also been extensively reported as a sensing material. Li et al. utilized Ru–doped  $\text{SnO}_2$  for acetone gas sensing. The electron depletion layer formed at the p–n heterojunction resulted in more chemisorbed oxygen species and further improved the gas–sensing performance [29]. Among all reported nanoscale materials, the electrospun fiber with a large specific surface area has been widely used to develop as sensing materials. Qiu et al. demonstrated a conductive film for detecting vital bio–signals. The conductive film consisted of annealed electrospun phenolic resin fibers on graphene which is then semi–embedded into a styrene–ethylene–butylene–styrene (SEBS) elastomer. The high–temperature annealing process creates strong interactions between the polymer fibers and graphene, resulting in a network that mimics the structure of a bird’s nest [30]. The electrospinning method allows diversity in material selection and preparation methods. Solution properties, operating parameters, and environmental conditions are crucial factors in the morphology of electrospun nanofibers. Incorporating functional nanoparticles into electrospun fibers can expand the applicability of the materials.

In this study, we developed highly sensitive tungsten oxide/tin oxide/silver/poly (methyl methacrylate) ( $\text{WO}_3/\text{SnO}_2/\text{Ag}/\text{PMMA}$ ) sensing materials to detect acetone in exhaled breath. It takes advantage of the distinct optical property of  $\text{WO}_3$ ,  $\text{SnO}_2$ , and Ag surface plasmon resonance. The correlation between the sensitivity and UV–ozone etching treatment on the  $\text{WO}_3/\text{SnO}_2/\text{Ag}/\text{PMMA}$  sensing materials was investigated to understand the modulation of VOC sensitivity. By monitoring the evolution of sensing materials’ extinction spectra, low concentrations of acetone gas can be detected. It is hoped that the enhanced sensitivity and accuracy of sensing materials can be used to identify early–diabetic patients, reduce the waste of medical resources, and enhance the quality of life for patients.

## 2. Materials and Methods

### 2.1. Preparation of Freestanding $\text{WO}_3/\text{SnO}_2/\text{Ag}/\text{PMMA}$ Sensing Materials

Silver nanoparticles (Ag NPs) were synthesized using solution–based chemical reduction routes as reported by Polavarapu et al. [31]. Silver nitrate ( $\text{AgNO}_3$ , >99.5%, Sigma–Aldrich) was used as a precursor and oleylamine ( $\text{C}_{18}\text{H}_{37}\text{N}$ , >98%, Sigma–Aldrich) was used as a reducing agent. Ag NPs were obtained by dissolving 0.6 mmol of  $\text{AgNO}_3$  and 6.0 mmol of oleylamine in 50.0 mL of chlorobenzene ( $\text{C}_6\text{H}_5\text{Cl}$ , >99%, Acros) in a four–necked flask. The reaction mixture was kept at 120 °C for 1 h with continuous stirring under a nitrogen atmosphere and then cooled down to room temperature. The Ag NPs were dispersed in chlorobenzene and further materials during fabrication.  $\text{SnO}_2$  NPs were synthesized by hydrothermal method. An amount of 0.53 g of  $\text{SnCl}_4 \cdot 5\text{H}_2\text{O}$  (>98.0%, Nacalai Tesque) was dissolved in 10 mL of benzyl alcohol ( $\text{C}_7\text{H}_8\text{O}$ , 99%, ACROS) with continuous stirring for 10 min. The mixture was transferred into a Teflon–lined autoclave and placed inside a 120 °C oven for 12 h. The resulting  $\text{SnO}_2$  NPs were centrifuged at 5000 rpm for 10 min and washed three times with diethyl ether.  $\text{WO}_3$  was synthesized by the solvent–thermal method. Tungsten chloride ( $\text{WCl}_6$ , 99.9+%, ACROS) was used as the soluble tungsten source and

ethanol was used as the solvent.  $WCl_6$  (50.0 mg) was added to 40.0 mL of ethanol ( $C_2H_6O$ , 95%, ACROS) and stirred for 30 min. The mixture was transferred into a Teflon-lined autoclave and placed in a 180 °C oil bath for 12 h. The resulting  $WO_3$  NPs were centrifuged at 5000 rpm for 15 min and washed three times with DI water.

To prepare  $WO_3/SnO_2/Ag/PMMA$  sensing materials, the electrospinning precursor solution was prepared by dissolving various ratios of 1.0 wt% Ag, 1.0 wt%  $SnO_2$ , 1.5 wt%  $WO_3$ , and 5.0 wt% PMMA in dimethylformamide (DMF,  $C_3H_7NO$ , >99.5%, Fisher Scientific). PMMA (MW~120,000 Da) was purchased from Sigma–Aldrich and used without further purification. The  $WO_3/SnO_2/Ag/PMMA$  precursor solution was stirred at 80 °C for 3 h until the polymer was completely dissolved. Then, the  $WO_3/SnO_2/Ag/PMMA$  nanofibers were fabricated using the electrospinning technique from the precursor solution mentioned above. The electrospinning device includes a syringe pump (KDS–100, KD Scientific Inc., Holliston, MA, USA), a high–voltage power supply (SC–PME50, Cosmi Global Co. Ltd., New Taipei City, Taiwan), and a grounded rotary collector with a diameter of 15.0 cm and a length of 15.0 cm (FES–COS, Falco Tech Enterprise Co. Ltd., New Taipei City, Taiwan). The optimized electrospun parameters in the operation were an applied voltage of 10.0–25.0 kV, a working distance of 10.0 cm, a flow rate of 0.5 mL/h, a solution volume of 10 mL, and a receiving plate speed of 500 rpm. For the surface treatment of sensing materials,  $WO_3/SnO_2/Ag/PMMA$  hybrid fiber was subjected to a 10 min surface etching treatment by ultraviolet light/ozone etching technology (UV/Ozone, IAST0001–020, STAREK Scientific Co., Taipei City, Taiwan) to increase its surface area. The UV/Ozone was equipped with 4 UVC lamps (PL–L, 36W,  $\lambda_{max} = 254$  nm, Philips, Amsterdam, Netherlands).

## 2.2. Material Characterization

The microstructures of Ag NPs,  $SnO_2$  NPs, and  $WO_3$  NPs were observed by using the transmission electron microscope (TEM, JEM–2100Plus, JEOL, Tokyo, Japan). The percentage distribution of particles' sizes was obtained from individual measurements of at least 100 particles. UV–vis absorption spectra of various nanoparticles were measured by a UV–VIS spectrophotometer (UV–1900i, Shimadzu, Kyoto, Japan). For the morphology of various sensing material, field–emission scanning electron microscope (FESEM, model SU8010, Hitachi, Tokyo, Japan) were used for the observation. At least 100 fibers were counted for obtaining fiber diameter distribution.

## 2.3. Optical Measurement of Extinction Spectrum

The VOCs were injected into a 4.5 cm by 4.0 cm by 4.0 cm quartz glass container to simulate the concentration of breath acetone. Measurements are taken at room temperature (25 °C) with a relative humidity range of 60%. To prevent the interference of environmental humidity, the response time is defined as extinction change value exceeding the extinction change maximum ( $\Delta E_{max}$ ) of blank (air). Namely, as the  $\Delta E$  that is over the threshold of the  $\Delta E_{max, air}$ . In the beginning, the  $WO_3/SnO_2/Ag/PMMA$  sensing material was placed in the middle of the container. The target solvent with a specific concentration was injected into the quartz chamber and the extinction spectrum was measured every 30 s immediately. The extinction spectrum was measured by UV–VIS spectrophotometer from the wavelength 400 nm to 1000 nm. The maximum extinction change ( $\Delta E$ ) of the peak is determined as the sensitivity for a particular VOC. The absorption behavior of the sensing material results in a variety of extinction intensities. Therefore, the extinction change of the peak is defined by the extinction before and after the VOC sensing. The extinction formula is defined as follows

$$\Delta E = E_t - E_{t_0}$$

where  $E_{t_0}$  represents the extinction intensity of the peak before the VOCs detection and  $E_t$  represents the extinction intensity of the peak after the VOCs detection.

### 3. Results

To specifically identify acetone, a diabetic breath biomarker, three nanoparticles, including Ag, SnO<sub>2</sub>, WO<sub>3</sub>, were chosen as sensing materials to enhance the acetone detection sensitivity. The schematic showing the preparation of the WO<sub>3</sub>/SnO<sub>2</sub>/Ag/PMMA sensing materials is shown in Figure 1a. The fibrous films were prepared through electrospinning technique using the WO<sub>3</sub>/SnO<sub>2</sub>/Ag/PMMA hybrid solution in DMF. The microstructures and size distribution of the synthesized Ag, SnO<sub>2</sub>, and WO<sub>3</sub> were investigated by TEM. The TEM images exhibited uniformly mono-dispersed spherical Ag NPs. The histogram of the size distribution showed an average spherical Ag NPs size of 10 nm (Figure 1(b-1,b-2)). The UV–visible spectrum of the Ag NPs showed an absorption peak at around 430 nm (Figure 1(b-3)). Due to the surface plasmon resonance effect (SPR), Ag NPs usually absorb light noticeably and intensely at a specific wavelength between 400–450 nm. Thus, the introduction of Ag NPs into the sensing material is expected to increase the sensitivity of the gas sensing effectively. The TEM image of SnO<sub>2</sub> NPs Figure 1(c-1,c-2) clearly indicates the successful synthesis of small nanodimensional spherical SnO<sub>2</sub> NPs with an average diameter of 17 nm. The absorption edge of SnO<sub>2</sub> NPs was located at around 390 nm (Figure 1(c-3)). Spherical WO<sub>3</sub> NPs can be observed through the TEM image in Figure 1(d-1). The histogram of size distribution calculated from the TEM image shows an average diameter of 18 nm (Figure 1(d-2)). The absorption edge of WO<sub>3</sub> NPs was located at around 490 nm (Figure 1(d-3)). Considering the advantages of Ag, SnO<sub>2</sub>, and WO<sub>3</sub> NPs, the designed WO<sub>3</sub>/SnO<sub>2</sub>/Ag/PMMA sensing material is expected to enhance the sensitivity of VOCs sensing.

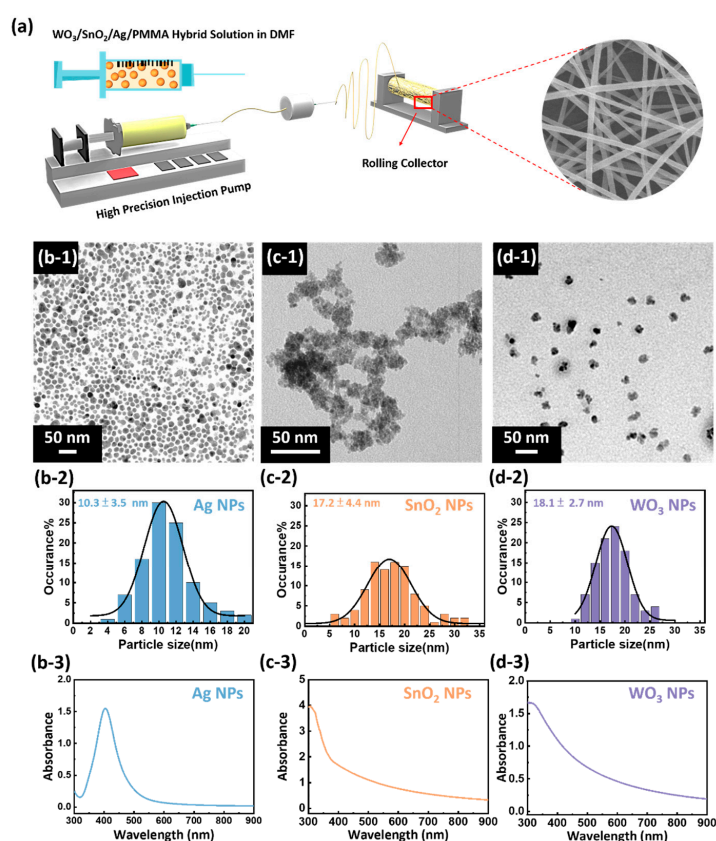


**Figure 1.** (a) The schematic of sensing material preparation. (b-1,c-1,d-1) TEM image, (b-2,c-2,d-2) the percentage distribution of particles sizes, and (b-3,c-3,d-3) UV–vis absorbance spectrum of (b-1,b-2,b-3) Ag NPs, (c-1,c-2,c-3) SnO<sub>2</sub> NPs, (d-1,d-2,d-3) WO<sub>3</sub> NPs.

Both the applied voltage and working distance have been shown to have varying effects on fiber diameter. Here, SnO<sub>2</sub>/Ag/PMMA (Figure 2a–c), WO<sub>3</sub>/Ag/PMMA (Figure 2e–g) and WO<sub>3</sub>/SnO<sub>2</sub>/Ag/PMMA (Figure 2i–k) fibers with various applied volt-

age were deposited on glass substrates to understand the effect on the surface morphology and optical properties. An electric field is formed between the spinneret nozzle and the grounded collector by applying a voltage of 10 kV (Figure 2a,e,i), 15 kV (Figure 2b,f,j), and 20 kV (Figure 2c,g,k), respectively. The diameter distribution of nanofibers are presented in Figure 2d,h,l and summarized in Table 1. It is established that the diameter of nanofibers decreased as the voltage increased. The appropriate voltage could ensure the formation of a stable Taylor cone for uniform electrospun fibers [32,33]. Fundamentally, reducing the fiber diameter increases the specific surface area, leading to stronger VOCs absorption behavior. The smallest diameter of SnO<sub>2</sub>/Ag/PMMA, WO<sub>3</sub>/Ag/PMMA and WO<sub>3</sub>/SnO<sub>2</sub>/Ag/PMMA fibrous film was produced using an applied voltage of 20 kV. However, these nanofibers showed irregular diameter distributions, which hindered the reproducibility and reliability of the sensor. Therefore, we chose the optimal voltage—10 kV for SnO<sub>2</sub>/Ag/PMMA and 15 kV for WO<sub>3</sub>/Ag/PMMA and WO<sub>3</sub>/SnO<sub>2</sub>/Ag/PMMA—that produced the most uniformly distributed fibers for sensing material production.

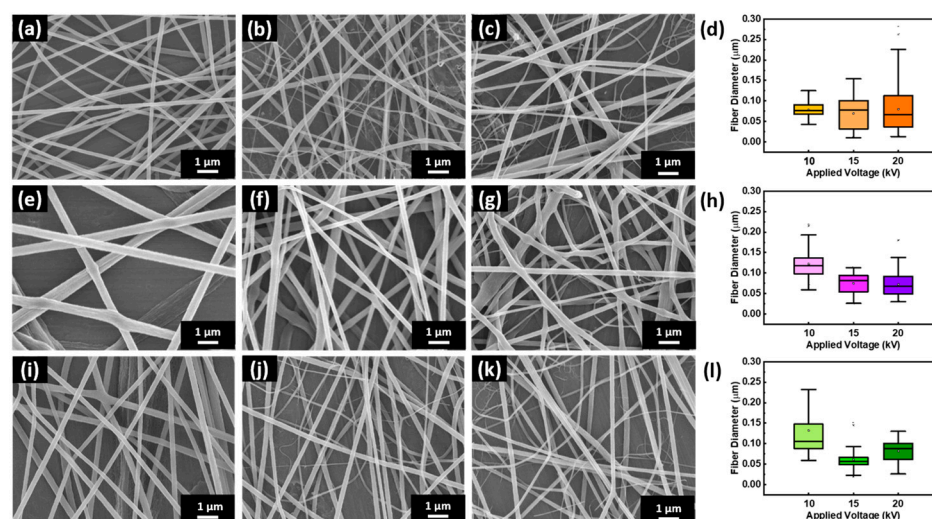


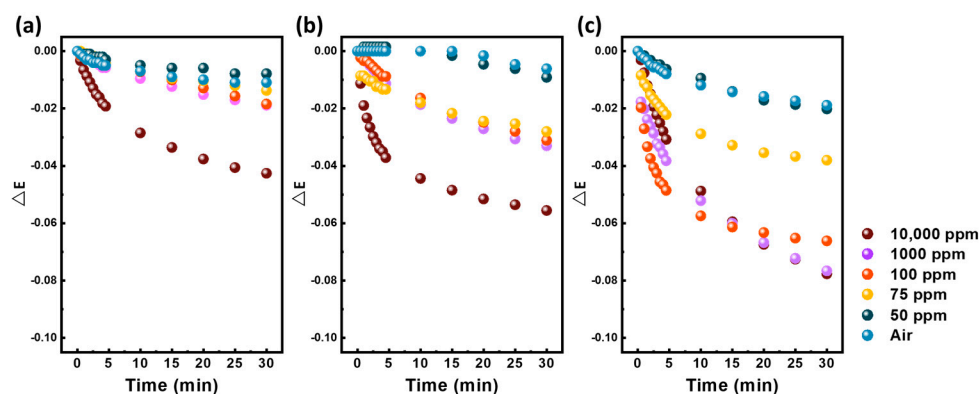
**Figure 2.** SEM images and boxplot of fiber diameter distribution of electrospun fibers: (a–d) SnO<sub>2</sub>/Ag/PMMA, (e–h) WO<sub>3</sub>/Ag/PMMA, and (i–l) WO<sub>3</sub>/SnO<sub>2</sub>/Ag/PMMA. Electric field: (a,e,i) 10 kV, (b,f,j) 15 kV, and (i,j,k) 20 kV. The boxplots show medians, interquartile ranges and outliers.

**Table 1.** Average diameter of SnO<sub>2</sub>/Ag/PMMA, WO<sub>3</sub>/Ag/PMMA and WO<sub>3</sub>/SnO<sub>2</sub>/Ag/PMMA fibers with various applied voltage.

Sample	Applied Voltage (kV)	Fiber Diameter (nm)
SnO <sub>2</sub> /Ag/PMMA	10	78 ± 16
	15	69 ± 38
	20	80 ± 54
WO <sub>3</sub> /Ag/PMMA	10	122 ± 32
	15	75 ± 23
	20	72 ± 30
WO <sub>3</sub> /SnO <sub>2</sub> /Ag/PMMA	10	132 ± 68
	15	61 ± 22
	20	82 ± 26

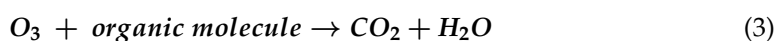
Figure 3 shows the extinction change of SnO<sub>2</sub>/Ag/PMMA, WO<sub>3</sub>/Ag/PMMA and WO<sub>3</sub>/SnO<sub>2</sub>/Ag/PMMA, when exposed to various concentrations of acetone. A control experiment using water simulates the moisture in the background (i.e., air) and is used as a relative reference to avoid detection mistakes. Based on our previous work, we have found that PMMA mixing with Ag NPs can efficiently enhance the detection limit of the sensing material from surface plasmon resonances. However, the detection limit of the Ag/PMMA

sensing material could only reach 100 ppm acetone vapor (Figure S1). Therefore, we further introduced SnO<sub>2</sub> to increase selectivity and WO<sub>3</sub> to take advantage of its gasochromic property. It can be observed that the addition of SnO<sub>2</sub> actually decreased the response intensity instead of increasing it. For the WO<sub>3</sub>/Ag/PMMA sensing material, the detection limit was also reduced to 75 ppm. However, the WO<sub>3</sub>/SnO<sub>2</sub>/Ag/PMMA sensing material demonstrated a synergistic effect, greatly increasing the extinction change and shortening the response time. Moreover, both SnO<sub>2</sub> and WO<sub>3</sub> are n-type semiconductors. The interfaces between SnO<sub>2</sub> and WO<sub>3</sub> might construct n–n junctions, where a part of W<sup>6+</sup> ions will substitute Sn<sup>4+</sup> ions in SnO<sub>2</sub> through n–type doping. Therefore, it would generate more electron–hole pairs than those without such structure when the light strikes [34]. This helps to improve the sensitivity of sensing materials when they are subjected to acetone surroundings.



**Figure 3.** Extinction changes of (a) SnO<sub>2</sub>/Ag/PMMA fibers (b) WO<sub>3</sub>/Ag/PMMA and (c) WO<sub>3</sub>/SnO<sub>2</sub>/Ag/PMMA sensing materials exposed to various concentrations of acetone.

To increase the specific surface area of the WO<sub>3</sub>/SnO<sub>2</sub>/Ag/PMMA sensing materials, we etched the specimen's surface with UV–ozone for 10 min. It is noteworthy to observe the morphological changes in the SEM images (Figure 4a,b). The surface area of the WO<sub>3</sub>/SnO<sub>2</sub>/Ag/PMMA sensing materials gradually eroded when etched and further enriched the specific surface area. We infer that the sensitivity of the sensing material is related to the specific surface area of the WO<sub>3</sub>/SnO<sub>2</sub>/Ag/PMMA sensing materials. To investigate the effect of UV–ozone treatment, the sensing material with and without etching were exposed to a concentration of 10,000 ppm acetone vapor for 30 min (Figure 4c). The extinction change shows a noticeable improvement after UV–ozone treatment. This is attributed to the deformation of the electrospun fibers. The etched fibers became fragile and easily reacted with VOCs. Besides, the UV–ozone is a simple and effective method for increasing the hydrophilicity of the sensing material to enhance the VOCs adsorption behavior. The schematic diagram of UV–ozone mechanism is shown in Figure 4d. Driven by the UV radiation, oxygen molecules (O<sub>2</sub>) dissociate and split into oxygen radicals (O·). These oxygen radicals recombine with oxygen molecules to form ozone (O<sub>3</sub>). At the same time, O<sub>3</sub> reacts with organic molecules absorbed by the substrate to form carbon dioxide (CO<sub>2</sub>) and water (H<sub>2</sub>O), which leave the substrate during the UV–ozone treatment. Next, driven by the UV radiation, the formation of hydroxyl radicals (·OH) by ozone photolysis provides a chemically active surface for VOCs adsorption [35,36].



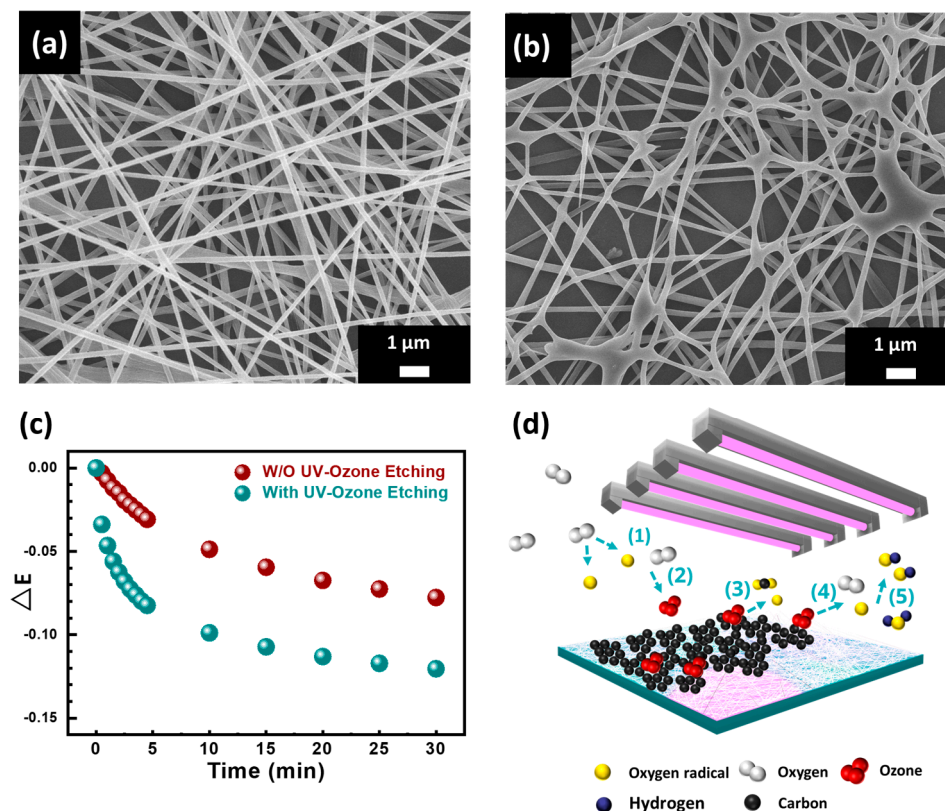


**Figure 4.** SEM images of  $WO_3/SnO_2/Ag/PMMA$  with UV–ozone etching: (a) non–etched and (b) 10 min etched. (c) Extinction changes of  $WO_3/SnO_2/Ag/PMMA$  sensing materials with and without etching when exposed to 10,000 ppm acetone. (d) Schematic diagram of UV–ozone etching process.

The  $WO_3/SnO_2/Ag/PMMA$  sensing material was successfully prepared by adjusting the fiber diameter and UV–ozone etching. The surface area of the sensing material can be effectively increased from the surface treatment, showing a good adsorption effect on VOCs. We suggest that the etched fibers were too fragile to maintain their shape, resulting in a shortened response time. In addition to detecting the acetone biomarker, we also detected other common VOCs in the industry, ethanol, p–Xylene, and toluene. The extinction spectra and response time are summarized in Figure 5 and Table 2. The developed sensing material can detect 20 ppm acetone vapor within 10 min. Toluene and xylene can both be effectively sensed at 80 ppm. The result from ethanol showed that the detection limit of ethanol can reach 100 ppm. The conversion of a hydrophobic surface to a hydrophilic surface after UV–ozone treatment can have several effects on the behavior of chemical species that interact with that material surface. In the case of toluene and p–Xylene, which are both hydrophobic, the hydrophilic surface generated by UV–ozone treatment could potentially reduce their affinity for the sensor surface. The change in surface chemistry induced by the UV–ozone treatment may also affect the kinetics of adsorption and desorption of toluene and p–Xylene on the sensor surface. Hydrophilic surfaces typically exhibit faster adsorption rates for polar or charged molecules, which could lead to shorter response times for these species, such as acetone and ethanol, in a sensor application. Figure S2 illustrates the error bars chart of the extinction change of the  $WO_3/SnO_2/Ag/PMMA$  sensing material under each exposing concentration, calculated

through three tests. Few deviations were observed in the extinction change curve during the detection of acetone at concentrations of 10,000, 1000, and 100 ppm. This indicates the high reliability of  $WO_3/SnO_2/Ag/PMMA$  sensing materials when using the developed technique. In addition, the as-fabricated acetone sensor performances in this paper were compared with that of other sensors, as shown in Table 3. Most of the sensors, such as conductometric and chemiresistive sensors, which perform optimally under high temperatures and are susceptible to humidity, can reach a ppb level detection. Exhaled breath preconcentration is a procedure in which exhaled breath samples are concentrated to increase the sensitivity of subsequent analyses. For improving the detection performance, preconcentration could be a way to improve the detection limit of analytical instruments by increasing the concentration of the target analytes and reducing the interference from other components in the breath sample. The  $WO_3/SnO_2/Ag/PMMA$  sensing material still demonstrates unique performance, including high sensitivity, low-cost, and operation at room temperature.

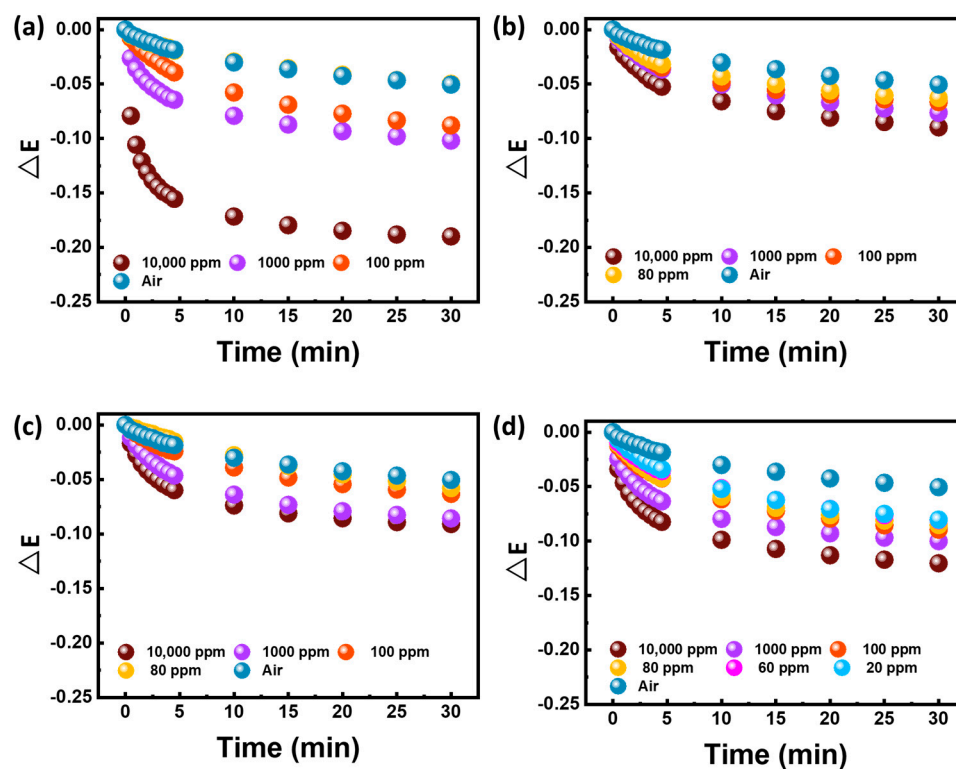


Figure 5. Extinction changes of the  $WO_3/SnO_2/Ag/PMMA$  sensing materials exposed to various concentrations of (a) ethanol, (b) p-Xylene, (c) toluene, and (d) acetone.

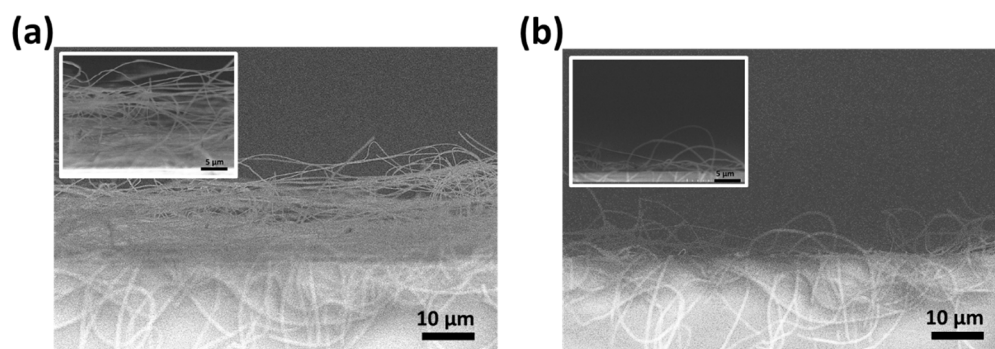
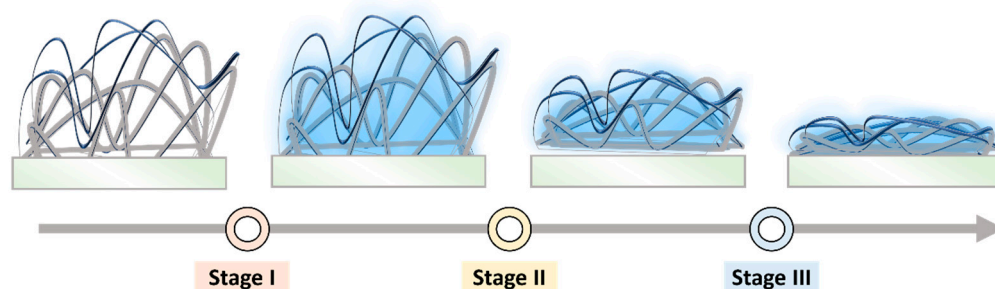
Table 2. Detection limit and response time of the  $WO_3/SnO_2/Ag/PMMA$  sensing materials when exposed to various VOCs concentrations.

VOCs	Detection Limit (ppm)	$\Delta E$	Responses Time (min)
Ethanol	100	−0.087	10
p-Xylene	80	−0.061	20
Toluene	80	−0.058	25
Acetone	20	−0.081	10

**Table 3.** Acetone sensing properties of with various types of reported sensing materials.

Materials	Sensor Type	Detection Limit	Detection Time	Operation Temp. (°C)	Ref.
WO <sub>3</sub> –In <sub>2</sub> O <sub>3</sub>	conductometric	0.1 ppm	real–time	280	[37]
SnSe <sub>2</sub> /SnO <sub>2</sub>	conductometric	0.354 ppm	real–time	300	[38]
γ–WO <sub>3</sub>	chemiresistive	0.2 ppm	20 s	300	[39]
N–doped carbon dots	colorimetric	0.5 mM	–	room temperature	[40]
Co <sub>3</sub> O <sub>4</sub> –TiO <sub>2</sub>	conductometric	0.1 ppm	122 s	250	[41]
Ru–Co <sub>3</sub> O <sub>4</sub>	conductometric	50 ppb	real–time	137.5	[42]

In order to verify the nanostructures of our sensing material and establish the sensing mechanism, FESEM was carried out. Figure 6 demonstrates the cross–sectional FESEM images of WO<sub>3</sub>/SnO<sub>2</sub>/Ag/PMMA sensing materials before and after exposure to acetone. Prior to exposure, the electrospun fiber gave the surface a 3D structure. After exposure to VOC environment, the fiber exhibited obvious collapse behavior. Based on our observations, we developed a hypothesis for the sensing mechanism of the material. For the developed sensing material, the sensing behavior can be divided into three stages as illustrated in Figure 7. In stage I, when the sensing material is exposed to VOCs in the surroundings, the hydrophilic surface of the sensing material readily adsorbs the VOCs present in the environment onto the 3D fibrous film. This is due to the increased affinity of the hydrophilic surface to acetone after UV–ozone treatment. In the stage II, the adsorbed VOCs cause polymer relaxation or swelling of the fibrous film, which leads to the collapse of the fibrous structure. This collapse might be due to changes in the intermolecular forces between the polymer chains, which can result from the presence of the adsorbed VOCs. Finally, the fibers of the sensing material experience over–swelling, which results in the complete collapse of the 3D fibrous structure. This collapse causes the disappearance of the 3D scattering effect, which is a key feature of the sensing material’s response to VOCs.

**Figure 6.** The cross–sectional FESEM images of WO<sub>3</sub>/SnO<sub>2</sub>/Ag/PMMA sensing materials (a) before and (b) after being exposed to acetone.**Figure 7.** Schematic diagram of the VOC sensing behavior.

#### 4. Conclusions

WO<sub>3</sub>/SnO<sub>2</sub>/Ag/PMMA sensing materials were successfully synthesized by the electrospinning technique. Signal enhancement by Ag NPs can enhance the sensitivity of the developed sensing materials. Besides, by constructing the heterostructure of SnO<sub>2</sub> and WO<sub>3</sub>, we can utilize their selectivity and gasochromic property, respectively. The interfaces between SnO<sub>2</sub> and WO<sub>3</sub> might construct n–n junctions, which generate more electron–hole pairs than those without such structure when the light strikes. This helps to improve the sensitivity of sensing materials when they are subjected to acetone surroundings. The specific surface area was successfully increased after the UV–ozone treatment. The etched fibers were too fragile to maintain their shape and easily reacted with VOCs, resulting in increased sensitivity and a shortened response time. The developed WO<sub>3</sub>/SnO<sub>2</sub>/Ag/PMMA sensing material can detect 20 ppm acetone vapor within 10 min under room temperature. It is hoped that the developed sensing material can have a great impact on the development of sensors to reduce the frequency and stress of invasive testing for diabetic patients.

**Supplementary Materials:** The following supporting information can be downloaded at: <https://www.mdpi.com/article/10.3390/polym15081833/s1>, Figure S1: Extinction changes of Ag/PMMA fibers sensing materials when exposed to various concentrations of acetone; Figure S2: Repeatability of the WO<sub>3</sub>/SnO<sub>2</sub>/Ag/PMMA sensing materials exposed to acetone with various concentration.

**Author Contributions:** Y.-H.C.: Formal analysis, Investigation, Writing—original draft, T.-H.H., K.-C.H. and T.-H.L.: Formal analysis, Investigation. K.-H.H. and M.-C.W.: Conceptualization, Methodology, Writing—Review & Editing, Funding acquisition, Supervision. All authors have read and agreed to the published version of the manuscript.

**Funding:** The financial support from the National Science and Technology Council, Taiwan (Project No. 111-2628-E-182-001-MY2, and 111-2221-E-182-040-MY3), Chang Gung University (QZRPD181) and Chang Gung Memorial Hospital at Linkou (CMRPD2L0082 and BMRPC74) are highly appreciated.

**Institutional Review Board Statement:** Not applicable.

**Informed Consent Statement:** Not applicable.

**Data Availability Statement:** The data presented in this study are available on request from the corresponding author.

**Acknowledgments:** The authors appreciate Ming-Tao Lee (BL-13A1), Jyh-Fu Lee (BL-17C1) and Ting-Shan Chan (BL-01C1) at National Synchrotron Radiation Research Centre for their useful discussion and suggestions, and Y.-M. Chang at Instrumentation Centre of National Tsing Hua University for the TEM analysis. The authors also thank the Microscopy Center at Chang Gung University for their technical assistance.

**Conflicts of Interest:** The authors declare no conflict of interest.

#### References

1. Tan, Y.; Shu, Z.; Zhou, J.; Li, T.; Wang, W.; Zhao, Z. One-step synthesis of nanostructured g-C<sub>3</sub>N<sub>4</sub>/TiO<sub>2</sub> composite for highly enhanced visible-light photocatalytic H<sub>2</sub> evolution. *Appl. Catal. B* **2018**, *230*, 260–268. [CrossRef]
2. Victor, F.M.; de Lima Andrade, S.R.; Bandeira, F. Diabetic Ketoacidosis and Hyperosmolar Hyperglycemic State. In *Endocrinology and Diabetes: A Problem Oriented Approach*; Bandeira, F., Gharib, H., Griz, L., Faria, M., Eds.; Springer International Publishing: Cham, Switzerland, 2022; pp. 355–362.
3. Chreitah, A.; Hijazia, K.; Doya, L.; Salloum, A. Severe dyslipidemia associated with diabetic ketoacidosis in newly diagnosed female of type 1 diabetes mellitus. *Oxf. Med. Case Rep.* **2021**, *2021*, omab036. [CrossRef] [PubMed]
4. Elgenidy, A.; Awad, A.K.; Saad, K.; Atef, M.; El-Leithy, H.H.; Obiedallah, A.A.; Hammad, E.M.; Ahmad, F.-A.; Ali, A.M.; Dailah, H.G.; et al. Incidence of diabetic ketoacidosis during COVID-19 pandemic: A meta-analysis of 124,597 children with diabetes. *Pediatr. Res.* **2022**, 1–12. [CrossRef] [PubMed]
5. Kolb, H.; Kempf, K.; Röhlings, M.; Lenzen-Schulte, M.; Schloot, N.C.; Martin, S. Ketone bodies: From enemy to friend and guardian angel. *BMC Med.* **2021**, *19*, 313. [CrossRef] [PubMed]
6. McMichael, L.E.; Heath, H.; Johnson, C.M.; Fanter, R.; Alarcon, N.; Quintana-Diaz, A.; Pilolla, K.; Schaffner, A.; Jelalian, E.; Wing, R.R.; et al. Metabolites involved in purine degradation, insulin resistance, and fatty acid oxidation are associated with prediction of Gestational diabetes in plasma. *Metabolomics* **2021**, *17*, 105. [CrossRef] [PubMed]

7. Obeidat, Y. The Most Common Methods for Breath Acetone Concentration Detection: A Review. *IEEE Sens. J.* **2021**, *21*, 14540–14558. [[CrossRef](#)]
8. Ahmadipour, M.; Pang, A.L.; Ardani, M.R.; Pung, S.-Y.; Ooi, P.C.; Hamzah, A.A.; Mohd Razip Wee, M.F.; Aniq Shazni Mohammad Haniff, M.; Dee, C.F.; Mahmoudi, E.; et al. Detection of breath acetone by semiconductor metal oxide nanostructures-based gas sensors: A review. *Mater. Sci. Semicond. Process.* **2022**, *149*, 106897. [[CrossRef](#)]
9. Güntner, A.T.; Weber, I.C.; Schon, S.; Pratsinis, S.E.; Gerber, P.A. Monitoring rapid metabolic changes in health and type-1 diabetes with breath acetone sensors. *Sens. Actuators B Chem.* **2022**, *367*, 132182. [[CrossRef](#)]
10. Verma, A.; Yadav, D.; Singh, A.; Gupta, M.; Thapa, K.B.; Yadav, B.C. Detection of acetone via exhaling human breath for regular monitoring of diabetes by low-cost sensing device based on perovskite BaSnO<sub>3</sub> nanorods. *Sens. Actuators B Chem.* **2022**, *361*, 131708. [[CrossRef](#)]
11. Li, A.J.; Pal, V.K.; Kannan, K. A review of environmental occurrence, toxicity, biotransformation and biomonitoring of volatile organic compounds. *Environ. Chem. Ecotoxicol.* **2021**, *3*, 91–116. [[CrossRef](#)]
12. Yan, H.; Zhou, Y.-G. Electrical sensing of volatile organic compounds in exhaled breath for disease diagnosis. *Curr. Opin. Electrochem.* **2022**, *33*, 100922. [[CrossRef](#)]
13. Das, S.; Pal, M. Review—Non-Invasive Monitoring of Human Health by Exhaled Breath Analysis: A Comprehensive Review. *J. Electrochem. Soc.* **2020**, *167*, 037562. [[CrossRef](#)]
14. Prasanth, A.; Meher, S.R.; Alex, Z.C. Metal oxide thin films coated evanescent wave based fiber optic VOC sensor. *Sens. Actuators A Phys.* **2022**, *338*, 113459. [[CrossRef](#)]
15. Mohar, M. 2,4,7-Triaminofluorenone as a Multi-Analyte Colorimetric Sensor of Fluoride, Acetone Vapor, and Other Harmful Compounds. *ChemistrySelect* **2019**, *4*, 8061–8067. [[CrossRef](#)]
16. Bogireddy, N.K.R.; Sotelo Rios, S.E.; Agarwal, V. Simple one step synthesis of dual-emissive heteroatom doped carbon dots for acetone sensing in commercial products and Cr (VI) reduction. *Chem. Eng. J.* **2021**, *414*, 128830. [[CrossRef](#)]
17. Kumar, A.; Pawar, D.; Late, D.J.; Kanawade, R. PVA-coated miniaturized flexible fiber optic sensor for acetone detection: A prospective study for non-invasive diabetes diagnosis. *J. Mater. Sci. Mater. Electron.* **2022**, *33*, 2509–2517. [[CrossRef](#)]
18. Vadivel, S.; Balaji, G.; Rathinavel, S. High performance ethanol and acetone gas sensor based nanocrystalline MnCo<sub>2</sub>O<sub>4</sub> using clad-modified fiber optic gas sensor. *Opt. Mater.* **2018**, *85*, 267–274. [[CrossRef](#)]
19. Masikini, M.; Chowdhury, M.; Nemraoui, O. Review—Metal Oxides: Application in Exhaled Breath Acetone Chemiresistive Sensors. *J. Electrochem. Soc.* **2020**, *167*, 037537. [[CrossRef](#)]
20. Broza, Y.Y.; Vishinkin, R.; Barash, O.; Nakhleh, M.K.; Haick, H. Synergy between nanomaterials and volatile organic compounds for non-invasive medical evaluation. *Chem. Soc. Rev.* **2018**, *47*, 4781–4859. [[CrossRef](#)]
21. Zuo, H.; Li, Y.; Liao, Y. Europium Ionic Liquid Grafted Covalent Organic Framework with Dual Luminescence Emissions as Sensitive and Selective Acetone Sensor. *ACS Appl. Mater. Interfaces* **2019**, *11*, 39201–39208. [[CrossRef](#)]
22. Wang, D.; Zhang, F.; Prabhakar, A.; Qin, X.; Forzani, E.S.; Tao, N. Colorimetric Sensor for Online Accurate Detection of Breath Acetone. *ACS Sens.* **2021**, *6*, 450–453. [[CrossRef](#)] [[PubMed](#)]
23. Yoon, J.; Chae, S.K.; Kim, J.-M. Colorimetric Sensors for Volatile Organic Compounds (VOCs) Based on Conjugated Polymer-Embedded Electrospun Fibers. *J. Am. Chem. Soc.* **2007**, *129*, 3038–3039. [[CrossRef](#)] [[PubMed](#)]
24. Liu, H.; Wang, Y.; Mo, W.; Tang, H.; Cheng, Z.; Chen, Y.; Zhang, S.; Ma, H.; Li, B.; Li, X. Dendrimer-Based, High-Luminescence Conjugated Microporous Polymer Films for Highly Sensitive and Selective Volatile Organic Compound Sensor Arrays. *Adv. Funct. Mater.* **2020**, *30*, 1910275. [[CrossRef](#)]
25. Kau, N.; Jindal, G.; Kaur, R.; Rana, S. Progress in development of metal organic frameworks for electrochemical sensing of volatile organic compounds. *Results Chem.* **2022**, *4*, 100678. [[CrossRef](#)]
26. Li, H.-Y.; Zhao, S.-N.; Zang, S.-Q.; Li, J. Functional metal-organic frameworks as effective sensors of gases and volatile compounds. *Chem. Soc. Rev.* **2020**, *49*, 6364–6401. [[CrossRef](#)]
27. Kang, X.; Deng, N.; Yan, Z.; Pan, Y.; Sun, W.; Zhang, Y. Resistive-type VOCs and pollution gases sensor based on SnO<sub>2</sub>: A review. *Mater. Sci. Semicond. Process.* **2022**, *138*, 106246. [[CrossRef](#)]
28. Gautam, V.; Kumar, A.; Kumar, R.; Husain, M.; Jain, V.K.; Nagpal, S. Ultrafast trace-level detection of methyl nicotinate biomarker using TiO<sub>2</sub>/SiNWs nanocomposite-based sensing platform. *J. Mater. Sci. Mater. Electron.* **2022**, *33*, 3411–3423. [[CrossRef](#)]
29. Li, J.; Xian, J.; Wang, W.; Cheng, K.; Zeng, M.; Zhang, A.; Wu, S.; Gao, X.; Lu, X.; Liu, J.-M. Ultrafast response and high-sensitivity acetone gas sensor based on porous hollow Ru-doped SnO<sub>2</sub> nanotubes. *Sens. Actuators B Chem.* **2022**, *352*, 131061. [[CrossRef](#)]
30. Qiu, J.; Yu, T.; Zhang, W.; Zhao, Z.; Zhang, Y.; Ye, G.; Zhao, Y.; Du, X.; Liu, X.; Yang, L.; et al. A Bioinspired, Durable, and Nondisposable Transparent Graphene Skin Electrode for Electrophysiological Signal Detection. *ACS Mater. Lett.* **2020**, *2*, 999–1007. [[CrossRef](#)]
31. Polavarapu, L.; Liz-Marzán, L.M. Growth and galvanic replacement of silver nanocubes in organic media. *Nanoscale* **2013**, *5*, 4355–4361. [[CrossRef](#)]
32. Wang, S.; Yi, L.; Wang, L.; Yao, J.; Militky, J.; Venkataramam, M.; Wiener, J.; Zhang, M. Preparation of core-sheath nanofibers with high latent heat by thermal cross-linking and coaxial electrospinning. *Polymer* **2021**, *228*, 123958. [[CrossRef](#)]
33. Lei, S.; Quan, Z.; Qin, X.; Yu, J. Asymptotic decay of velocity of whipping jet in electrospinning. *Polymer* **2021**, *217*, 123456. [[CrossRef](#)]

34. Zhang, J.; Zhang, L.; Leng, D.; Ma, F.; Zhang, Z.; Zhang, Y.; Wang, W.; Liang, Q.; Gao, J.; Lu, H. Nanoscale Pd catalysts decorated WO<sub>3</sub>-SnO<sub>2</sub> heterojunction nanotubes for highly sensitive and selective acetone sensing. *Sens. Actuators B Chem.* **2020**, *306*, 127575. [[CrossRef](#)]
35. Fan, Z.; Zhi, C.; Wu, L.; Zhang, P.; Feng, C.; Deng, L.; Yu, B.; Qian, L. UV/Ozone-Assisted Rapid Formation of High-Quality Tribological Self-Assembled Monolayer. *Coatings* **2019**, *9*, 762. [[CrossRef](#)]
36. Choudhury, S.; Roy, S.; Bhattacharya, G.; Fishlock, S.; Deshmukh, S.; Bhowmick, S.; McLaughlign, J.; Roy, S.S. Potentiometric ion-selective sensors based on UV-ozone irradiated laser-induced graphene electrode. *Electrochim. Acta* **2021**, *387*, 138341. [[CrossRef](#)]
37. Hu, J.; Xiong, X.; Guan, W.; Long, H.; Zhang, L.; Wang, H. Self-templated flower-like WO<sub>3</sub>-In<sub>2</sub>O<sub>3</sub> hollow microspheres for conductometric acetone sensors. *Sens. Actuators B* **2022**, *361*, 131705. [[CrossRef](#)]
38. Jin, S.; Wu, D.; Song, W.; Hao, H.; Gao, W.; Yan, S. Superior acetone sensor based on hetero-interface of SnSe<sub>2</sub>/SnO<sub>2</sub> quasi core shell nanoparticles for previewing diabetes. *J. Colloid Interface Sci.* **2022**, *621*, 119–130. [[CrossRef](#)] [[PubMed](#)]
39. Americo, S.; Pargoletti, E.; Soave, R.; Cargnoni, F.; Trioni, M.I.; Chiarello, G.L.; Cerrato, G.; Cappelletti, G. Unveiling the acetone sensing mechanism by WO<sub>3</sub> chemiresistors through a joint theory-experiment approach. *Electrochim. Acta* **2021**, *371*, 137611. [[CrossRef](#)]
40. Alshareef, M.; Snari, R.M.; Alaysuy, O.; Aldawsari, A.M.; Abumelha, H.M.; Katouah, H.; El-Metwaly, N.M. Optical Detection of Acetone Using “Turn-Off” Fluorescent Rice Straw Based Cellulose Carbon Dots Imprinted onto Paper Dipstick for Diabetes Monitoring. *ACS Omega* **2022**, *7*, 16766–16777. [[CrossRef](#)]
41. Cai, Z.; Park, S. Highly selective acetone sensor based on Co<sub>3</sub>O<sub>4</sub>-decorated porous TiO<sub>2</sub> nanofibers. *J. Alloys Compd.* **2022**, *919*, 165875. [[CrossRef](#)]
42. Jin, R.; Jiang, Y.; Zhao, L.; Wang, T.; Liu, X.; Liu, F.; Yan, X.; Sun, P.; Lu, G. High sensitivity and low detection limit of acetone sensor based on Ru-doped Co<sub>3</sub>O<sub>4</sub> flower-like hollow microspheres. *Sens. Actuators B* **2022**, *363*, 131839. [[CrossRef](#)]

**Disclaimer/Publisher’s Note:** The statements, opinions and data contained in all publications are solely those of the individual author(s) and contributor(s) and not of MDPI and/or the editor(s). MDPI and/or the editor(s) disclaim responsibility for any injury to people or property resulting from any ideas, methods, instructions or products referred to in the content.